Materials Advances

ROYAL SOCIETY OF CHEMISTRY

REVIEW

View Article Online
View Journal | View Issue

Cite this: *Mater. Adv.*, 2021, **2**, 1190

Rare earth oxynitrides: promising visible-light-driven photocatalysts for water splitting†

Shijia Jiang, Yanxin Liu and Jun Xu *

Photocatalytic water splitting is a potential solution for the global energy crisis. However, most photocatalysts only respond to ultraviolet light irradiation, which is not the main component of sunlight. Photocatalysis driven by visible light has therefore become a challenging and cutting-edge research topic. In recent years, perovskite-type rare earth oxynitrides with a formula of ABO_xN_y (A = rare earth ions; B = Ti^{4+}, Zr^{4+}, Ta^{5+}, W^{6+}, etc.; $x + y = 3$) have been reported to be promising candidates for visible-light-driven photocatalytic water splitting. Several factors have been considered to be responsible, including (i) the combination of narrower band gap and higher water stability, (ii) flexible perovskite structure allowing the facile modulation of composition by single or multiple ion doping, (iii) the small differences in neighbouring rare earth elements making ultrafine tuning of properties possible, and (iv) the incorporation of additional functionalities arising from rare earth elements. Despite their importance, to the best of our knowledge, there is no review focusing on the progress of rare earth oxynitride photocatalysts yet. This review describes the proposed mechanism for photocatalytic water splitting, the synthetic methods of rare earth oxynitrides, their photocatalytic performances, the theoretically predicted phases, and the challenges and opportunities for future research on rare earth oxynitrides.

Received 7th November 2020,
Accepted 30th December 2020

DOI: 10.1039/d0ma00867b

rsc.li/materials-advances

1. Introduction

The global energy consumption increases with the growth of population and economy. Today, 90% of global energy comes from fossil fuels, and this number is expected to reach its maximum in 30 years.[1] Fossil energy is non-renewable. Combustion of fossil fuels has released a large amount of carbon dioxide into the atmosphere, leading to environmental issues such as the global climate change. In contrast, solar energy can be considered an inexhaustible resource. The earth's surface receives about 1.2×10^5 TW from solar radiation, which is equivalent to 130 million 500 MW power plants,[2] compared to the expected global energy consumption of 27 TW in 2050 and 43 TW in 2100.[3] Such a large difference suggests that the

Center for Rare Earth and Inorganic Functional Materials, Tianjin Key Lab for Rare Earth Materials and Applications, School of Materials Science and Engineering& National Institute for Advanced Materials, Nankai University, Tianjin, 300350, China. E-mail: junxu@nankai.edu.cn

† Electronic supplementary information (ESI) available. For ESI and crystallographic data in CIF or other electronic format see DOI: 10.1039/d0ma00867b

Shijia Jiang

Shijia Jiang is currently pursuing a master's degree at the School of Materials Science and Engineering, Nankai University. Her research interests are focused on rare-earth photocatalysts and solid-state NMR spectroscopy. In 2019, she received her BSc degree from Inner Mongolia University of Science and Technology, China.

Yanxin Liu

Yanxin Liu is currently pursuing a master's degree at the School of Materials Science and Engineering, Nankai University. His research interests are focused on layered rare-earth materials and solid-state NMR spectroscopy. In 2020, he received his BSc degree from Northeast Agricultural University, China.

utilization of only one ten-thousandth of the available solar energy can satisfy the global energy demand. Solar energy has thus attracted much attention because it is worthwhile, clean, and economical.[4]

However, the shortcomings of solar energy, such as low energy density and large fluctuations with time and region, usually require solar energy to be converted into other energy forms for practical applications, including electricity and chemical energy. Although the conversion from solar energy to electricity *via* solar cells is at a relatively mature stage, the storage of electricity is still an issue. As chemical energy is suitable for storage, converting solar energy to chemical energy has become an alternative strategy. In particular, photocatalytic water splitting produces hydrogen, which is an ideal clean and high-energy fuel.[5]

The phenomenon of photocatalysis has been recognized for a long time. Herein, we have to clarify that photocatalysis does not mean that light itself has a catalytic effect, but that the presence of a catalyst can accelerate the photochemical reaction.[6] In particular, photocatalytic water splitting refers to the decomposition of water to obtain H_2 and O_2 with a stoichiometric ratio of 2 : 1 under light. Photogenerated holes oxidize water to produce oxygen (*i.e.*, oxygen evolution reaction, OER), while photogenerated electrons reduce water to produce hydrogen (*i.e.*, hydrogen evolution reaction HER). As we have learned, ultraviolet (UV: <400 nm) light accounts for as little as 3% of the solar energy irradiated on the earth's surface, while the visible light energy (visible light: 400–760 nm) accounts for 44%. From the perspective of solar energy utilization, the visible-light-driven photocatalytic reaction surpasses the conventional UV-light-driven photocatalytic reaction. In such cases, even low-luminance indoor lighting sources can be utilized to generate hydrogen.[7]

Although metal oxides such as TiO_2 and ZnO are very successful photocatalysts for water splitting,[8] they are typically inactive under visible light irradiation due to their large bandgaps. It has been demonstrated that metal nitrides have smaller bandgaps due to the higher 2p orbital energy level of N^{3-} than that of O^{2-}.[9] However, the water stability of metal nitrides is poor, making them unsuitable for photocatalytic water splitting. Metal oxynitrides can simultaneously possess low bandgaps as metal nitrides and high stability in water as metal oxides, and thus have been developed as visible-light-driven photocatalysts for water splitting.[10–13]

During the recent renaissance of perovskites in a wide variety of applications such as in photovoltaic, luminescent, and photocatalytic materials, the large family of perovskite-type oxynitrides with a formula of ABO_xN_y (A = transition metal or rare earth ions; B = Ti^{4+}, Zr^{4+}, Ta^{5+}, W^{6+}, *etc.*; $x + y = 3$) has attracted considerable research interest. The perovskite structure is more flexible than a simple metal oxynitride structure, due to the inclination of the $BO_{6-x}N_x$ octahedral framework in various ways and the replacement of both A and B sites by many cations. Ionic doping/substitution has thus become an effective and robust approach for the fine tuning of physical and chemical properties. In particular, rare earth oxynitrides, which consist of fifteen lanthanide elements with unique electron configurations of $[Xe]4f^{n-1}5d^{0-1}6s^2$ (n = 1–15) and the elements Sc and Y, can possess even higher structural variability. It is because the changes in properties of neighboring rare earth elements, such as ionic radii, coordination behaviors, redox potentials, *etc.*, are significantly smaller than those of neighboring transition metals. Moreover, the unpaired 4f electrons of rare earth elements are typically not involved in chemical bonding, introducing unique magnetic, electronic, and luminescence functionalities into the oxynitrides. For example, because of magnetic anisotropy, spin–orbit coupling and crystal field effects, the paramagnetism of $RETiO_2N$ (RE = Ce, Pr, Nd) compounds deviates from the Curie–Weiss law below certain temperatures ($CeTiO_2N$: 150 K; $NdTiO_2N$: 30 K).[14] $EuWO_{1+x}N_{2-x}$ possesses colossal magnetoresistance when x is close to 0 and also shows excellent electronic flexibility, which is a promising candidate for new memory and sensor devices.[15] $LaTiO_2N$ films can display a high dielectric constant, which fluctuates greatly under the direct current (DC) electric field.[16] $LaTaON_2$ has excellent luminosity, tinting power, transparency and dispersibility, and thus can be used as non-toxic yellow-red pigments.[17] Although not reported to date, the interplay of these functionalities with photocatalysis may yield new families of multifunctional materials.

In recent years, the research interest of perovskite-type rare earth oxynitrides as visible-light-driven photocatalysts for water splitting has grown. However, to the best of our knowledge, there is still no review focusing on the progress in this emerging area. We are thus motivated to present a comprehensive review covering the mechanism of photocatalytic water splitting, the synthetic methods of rare earth oxynitrides, the photocatalytic activity, the theoretical predication of phases, and the challenges and opportunities for future research. We hope that this review will encourage more researchers to enter this field.

Jun Xu

Jun Xu is currently an associate professor at the School of Materials Science and Engineering, Nankai University. His research interests are focused on solid-state NMR spectroscopy and rare-earth functional materials. In 2008, he received his BSc degree from Peking University, China. In 2013, he received his PhD degree from the University of Western Ontario, Canada.

2. Mechanism of photocatalytic water splitting

The electronic structure of photocatalysts plays an important role in their performances.[18] For a solid, some of its electronic states

are empty and some are full. The full energy state and the empty energy state are referred to as the valence band (VB) and the conduction band (CB), respectively. If there is an energy difference between the VB and the CB (*i.e.*, a band gap), this material is a semiconductor or an insulator, depending on the size of the bandgap. A semiconductor may be used as a photocatalyst for water splitting, and the working principle is shown in Fig. 1.[19]

As illustrated in Fig. 1, the minimum value of the CB must be lower than the oxidation–reduction potential (ORP) of H^+/H_2 (0 V *vs.* NHE, NHE is the normal hydrogen electrode), and the maximum value of the VB must be higher than the ORP of O_2/H_2O (+1.23 V *vs.* NHE). The VB of metal oxides is mainly composed of O 2p orbitals. Their maximum values are thus much higher than +1.23 V *vs.* NHE, which leads to high photocatalytic water oxidation activity. However, the bandgap of metal oxides is usually so wide that they only respond to UV light. When O^{2-} is partially replaced with N^{3-}, *e.g.*, forming rare earth oxynitrides, the VB maximum (VBM) is composed of hybridized N 2p and O 2p orbitals, yielding smaller VBM and a narrower band gap. As a result, rare earth oxynitrides can absorb light with longer wavelengths and perform photocatalysis under visible light.

The three steps occurring in photocatalytic water splitting are the generation of electron–hole (e^-–h^+) pairs, the separation and migration of e^-–h^+ pairs, and the final chemical reaction with adsorbed surface species. In the ground state, all electrons are within the VB. After irradiation, the photocatalyst absorbs photons with energy higher than the bandgap energy to excite electrons from the VB into the CB, forming excited states and e^-–h^+ pairs. When these electrons and holes are separated and migrate to the surface of the catalyst, the redox reaction will proceed. The two protons needed to generate a H_2 molecule are reduced by the excited electrons in the photocatalyst. And the electrons generated by oxygen evolution can fill the holes in the valence band. The corresponding reaction formulae are shown in eqn (1) and (2).

$$\text{HER: } 2H^+ + 2e^- = H_2 \quad (1)$$

$$\text{OER: } H_2O + 2h^+ = 1/2O_2 + 2H^+ \quad (2)$$

However, the photo-generated electrons and holes are easily recombined and thus they may not migrate to the surface successfully. In such cases, the water splitting reaction will not occur. As a result, it is one of the key points to prevent the recombination of electrons and improve the photocatalytic activity. One of the very valuable approaches is to load co-catalysts such as Pt, Rh and CoO_x on the surface of photocatalysts. The co-catalyst can be considered to be equivalent to the counter electrode in the photoelectrochemical water splitting system, which reduces the recombination effectively. Every coin has two sides; it should be noted that if the co-catalysts are capable of promoting water formation, the O_2 and H_2 generated by water splitting simultaneously are easily recombined to generate water. The structures of the photocatalyst and co-catalyst thus need to be optimized to avoid the occurrence of reverse reactions.[11] More strategies to improve the photocatalytic activity will be presented in the following sections.

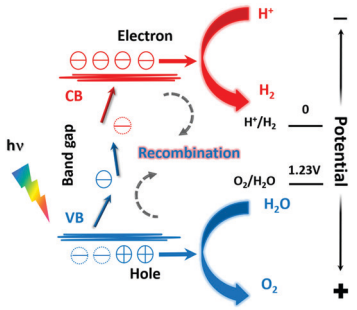

Fig. 1 A schematic diagram of the photocatalytic water splitting process.

3. Synthetic methods

The synthesis of oxynitrides is usually more challenging than oxides because of less stability and the requirement of a suitable nitriding agent to convert metal oxide precursors to oxynitrides (*i.e.*, the nitridation process). The most common nitridation process is the ammonolysis reaction with the following reaction formula:

$$\text{Metal-oxide} + NH_3 \rightarrow \text{metal-oxynitride} + H_2O\uparrow \quad (3)$$

It is evident that one of the most important factors governing the ammonolysis is the metal oxide precursor including its phase, composition, size, *etc.* Other factors such as temperature, gas flow rate, concentration, and pressure should also be optimized. In this section, the synthesis of precursors, nitridation, and fabrication of thin films and nanostructures are reviewed.

3.1. Synthesis of precursors

A suitable metal oxide precursor such as a ternary rare earth oxide consists of rare earth ions and transition metal ions mixed at the atomic level, resulting in shorter diffusion lengths and lower reaction temperatures.[20] Furthermore, the precursors prepared by different methods possess various sizes, morphologies, degrees of metal ion ordering, *etc.*, which can affect the nitridation process considerably.

3.1.1. Solid-state method. The solid-state method is the standard and most traditional way to synthesize ternary metal oxides. This method is very simple:[21] the corresponding binary oxides are mixed and dried at a stoichiometric ratio, and then sintered at a high temperature. The solid-state synthesis of $La_2Ti_2O_7$ is listed below (eqn (4)). However, the long diffusion path between particles of binary oxides makes the reaction very challenging (*e.g.*, very high reaction temperature) and the products less homogenous, which are not favorable for the subsequent nitridation reaction.

$$La_2O_3 + 2TiO_2 \xrightarrow{1500\ ^\circ C} La_2Ti_2O_7 \quad (4)$$

3.1.2. Co-precipitation method. To reduce the diffusion path and barrier between particles of binary oxides, the rare

earth ions and transition metal ions can be mixed in the precipitate of a solution. This method is very effective. For example, in the synthesis of $La_2Ti_2O_7$, the amorphous hydroxide is first formed by co-precipitation of a mixed solution of $TiCl_4$, RE_2O_3 (RE = rare earth), nitric acid and ammonia.[22] By further heating the amorphous hydroxide mixture, the desired $La_2Ti_2O_7$ is obtained. The reaction temperature is reduced to 800–1300 °C. The uniformity of $La_2Ti_2O_7$ powder can also be improved. However, the precipitation of different cations must be carefully controlled by adjusting the pH.[23] In addition, the co-precipitation process including nucleation, growth, coarsening and/or agglomeration is relatively complex and thus the product quality is controlled by many factors.[24]

3.1.3. Sol–gel method. The sol–gel process involves the preparation of a sol, formation of a wet gel, drying and calcination of the gel. Compared to the co-precipitation method, the mixing of multiple metal ions within gels is usually more homogenous, which can control the stoichiometry and uniformity better, reduce the reaction temperature, and make it easier to obtain ultra-fine powders, films and fibers.[25] Prasadarao *et al.* successfully synthesized $RE_2Ti_2O_7$ (RE = La, Nd) by the sol–gel method.[25] Lanthanum acetylacetonate ($La(acac)_3$) and titanium isopropoxide ($Ti[OCH(CH_3)_2]_4$) were used as starting materials and 2-methoxyethanol (MOE) was chosen as the solvent. The molar ratio of MOE/$La(acac)_3$ was maintained at about 80 by reflux, and the pH was adjusted to about 10. Water was added under stirring to make the solution transparent. The resulting sol–gel was dried in air at 60 °C and then heated at 700 °C. The obtained $La_2Ti_2O_7$ powder is phase pure.

3.1.4. Pechini method. The Pechini method can be regarded as an upgraded version of the sol–gel method. It was first reported by Pechini and colleagues back in 1967 and is extensively used to synthesize powder compounds.[24] In this method, the metal ion is first reacted with an organic chelating agent such as citric acid to form a complex, and a polyol such as ethylene glycol is then used to cause an esterification reaction with the chelate to form a gel. This method does not require a metal to form a suitable hydroxyl complex. In a relatively wide pH range, the chelating agent can form a stable complex with the metal, making it easier to synthesize fairly complex compounds. However, the size and micro-morphology of the powder cannot be well controlled. In addition, the combination of metal ions and organic matrix is very weak, which is not conducive to form two-dimensional chains and other specific structures, but usually forms spherical structures.

3.1.5. Polymerized-complex method. Later, a simpler and more time-saving method, *i.e.*, a polymerized-complex method, was developed.[26] This method is also referred to as the sol–gel auto-combustion method.[27] In this method, citric acid (CA) and ethylene glycol (EG) polymerize to form a polyester resin. The key to success is to screen out suitable experimental conditions so that during the resin formation process, no phase separation occurs and no insoluble hydroxides are formed.[28] Taking $RE_2Ti_2O_7$ as an example, the synthetic steps are as follows:[29] first, 0.01 mol of titanium isopropoxide was dissolved in 0.4 mol of EG. 0.3 mol of CA was then added under stirring. After CA is dissolved, 0.0105 mol (5% excess to Ti) of $RE(NO_3)_3{\cdot}nH_2O$ was added to the solution. Excessive RE^{3+} can inhibit the formation of TiO_2 rutile as an impurity. It has been reported that the TiO_2 rutile formed on the surface of $RE_2Ti_2O_7$ will reduce the photocatalytic activity.[30] The resulting solution was heated at about 130 °C to accelerate the esterification reaction. The obtained transparent brown resin was further reacted at 350 °C for 2 h, burned on an alumina plate at 800–1350 °C for 2–4 h, and finally cooled to room temperature to obtain powder $RE_2Ti_2O_7$. This method does not require very high temperature, and can yield a pure phase.

3.1.6. Hydrothermal method. The reaction conditions are typically milder in hydrothermal synthesis, and the size and morphology of the products can be more uniform.[31] Usually, equimolar amounts of the reactants are dissolved in deionized water, and then transferred to the reaction kettle after stirring. Depending on the reaction system, different reaction times and temperatures are used. After the reaction, the products are separated from the solution and finally dried. Chen *et al.* synthesized powdered pyrochlore and fluorite phase $La_2Zr_2O_7$ and perovskite phase $La_{2/3}TiO_{3-\lambda}$ (λ = 0–0.024) by the hydrothermal method, and then extensively explored the influence of various reaction conditions such as reaction temperature and reaction time on the particle size distribution and particle agglomeration.[32] The large difference of the ionic radii and chemistry of rare earth ions and transition metal ions is a challenge for hydrothermal synthesis. The hydrothermal method is also difficult to scale up.

3.1.7. Flux synthesis. The molten salt fluxes such as KCl/LiCl or Na_2SO_4/K_2SO_4 can be added to the mixture of binary oxides to reduce the reaction temperature of ternary oxides.[33] The resulting solid products are then washed with deionized water to obtain pure complex oxides. The advantages of flux synthesis are to obtain high purity products and uniform microstructures. This method is therefore expected to enable the study of morphology effects on photocatalytic activities by controlling the internal and surface structural characteristics of the crystal.

3.2. Nitridation

The stronger bonding within nitrogen molecules compared to oxygen molecules results in smaller free energy for the formation of oxynitrides. The rare earth oxynitrides are therefore obtained under harsher synthetic conditions than the ternary oxides. Nevertheless, various nitridation methods have been developed to convert oxides into oxynitrides.

3.2.1. Ammonolysis. As mentioned earlier, the most common method to synthesize oxynitrides is to place the oxide precursors in a NH_3 stream at high temperature. Parameters such as temperature, heating rate, and ammonia flow rate are very important.[34] The ammonolysis reaction temperature is usually 900–1500 °C at a heating rate of 10 °C min^{-1}. The specific temperature varies with the selected oxide precursor and reaction system.[35] The flow rate of the ammonia gas increases with the increase of reaction temperature, which helps in minimizing the

decomposition of ammonia gas to nitrogen and hydrogen gases before making contact with the precursor.[18]

Adding a molten salt flux during the nitridation process can promote the diffusion of atoms in precursor and nitrided materials, thereby achieving structural control of the final particles.[36] Maegli *et al.* added NaCl/KCl flux when synthesizing $LaTiO_2N$, and found that it had better crystallinity than samples without flux-assist.[37]

3.2.2. Methods without using NH_3. The traditional ammonolysis method to synthesize rare earth oxynitrides involves NH_3, which is dangerous and requires special exhaust gas treatments. Meanwhile, the reaction temperature is still high. Other nitridation agents such as urea,[38] amide[39] and azide[40] have been therefore used in recent years to obtain oxynitrides. Generally, this new method is to mix the precursor with urea, amide, azide, *etc.*, in an agate mortar at a certain molar ratio, transfer them to an alumina crucible boat, and then obtain the desired oxynitrides in a tube furnace filled with nitrogen rather than ammonia. This method can achieve lower reaction temperatures (900–1200 °C) and does not use NH_3. However, the experimental results showed that the oxide precursor must be prepared by the hydrothermal method and must contain $RE(OH)_3$ as a by-product. Only in this way, oxynitrides can be formed during the nitridation process.

Table 1 compares the advantages and disadvantages of various synthetic methods. Researchers should select their own synthetic routes according to their needs. To date, the most common synthetic method for oxide precursors is still the solid-state or derived methods, whereas ammonolysis is used to convert oxide precursors to rare earth oxynitrides.

3.3. Fabrication of thin films and nanostructures

3.3.1. Thin films. Rare earth oxynitrides obtained using the aforementioned methods are typically in powder form. However, the thin-film of oxynitrides has many advantages over powder such as good ductility and flexibility. Furthermore, it can be well applied in surface coating, photoelectric cells, *etc.*[35]

Physical deposition methods including sputter deposition and pulsed laser deposition have been used to fabricate thin films of rare earth oxynitrides. The fabrication of perovskite-type oxynitride $LaNbO_xN_y$ thin films uses LaN–NbN powder as the target, because it is difficult to prepare the deposited precursor target directly. Cohen *et al.* considered that a major drawback in this process is that the stoichiometry is difficult to control.[41] Lu *et al.* used $La_2Ti_2O_7$ powder as the target, and deposited $LaTiO_2N$ thin films in N_2 rich plasma by radio frequency magnetron sputtering technology.[16] Aguiar and co-workers[42] deposited $(La,Sr)TiO_{3+x/2}$ on $SrTiO_3$ and MgO targets by pulse laser deposition, and then obtained the corresponding oxynitrides $(La,Sr)Ti(O,N)_3$ by ammonolysis. Moreover, it was found that except for $x = 0.5$, in all other cases, the film grew along the (100) crystal orientation of the perovskite structure.

It is noteworthy that the thin films are basically obtained by epitaxial growth on the substrate and the lattice of the prepared material often appears to be mismatched with that of the substrate. In particular, for the perovskite structure films, in which the anion sequence often varies dramatically, the lattice mismatch of the film and substrate is quite common. As a result, the synthetic technology of thin films of rare earth oxynitrides still requires extensive exploration and improvement.[43]

3.3.2. Nanostructures. The synthesis of materials with nanostructures remains a hot topic to date. As shown in many works, the obtained nanomaterials often exhibit better performances than bulk materials or possess new features.[44,45]

Among the various methods, the template synthesis can easily control the shape, size, and even exposed crystal planes of nanoparticles. Li *et al.* first obtained carbon spheres through the hydrothermal reaction of glucose.[44] In the next step, they added carbon spheres into an ethanol solution of $LaCl_3$ and tetrabutyl titanate, allowing La^{3+} and Ti^{4+} to be absorbed on the surface of the carbon sphere. The carbon sphere was then removed through a calcination process to form hollow spherical $LaTiO_x$ precursors, and was finally successfully converted to $LaTiO_2N$ hollow nanospheres under NH_3 treatments. In another work,[45] Wang *et al.* first used the KOH/NaOH flux method to obtain plate-shaped $LaKNaTaO_5$ nanomaterials, and then directly nitridated them to evaporate K and Na species on the surface which resulted in the formation of $LaTaON_2$. Finally, the core–shell structured plate-shaped $LaKNaTaO_5/LaTaON_2$ was successfully synthesized. The photocatalytic activities of these two materials have been improved, which will be discussed in depth in the following section.

Besides the template synthesis, oriented attachment (OA) has been widely utilized to control the crystal growth *via* crystallographic alignment. A big challenge in OA crystallization is the removal of the additives, which is required to enable the OA assembling process. Yan *et al.* reported that the flux environment is an ideal medium for OA growth without additives.[46] Hundred-nanometer-size $LaTaON_2$ single crystals were first synthesized by conventional flux synthesis, which

Table 1 Evaluation table for the advantages and disadvantages of various synthetic methods

	Synthetic methods	Advantages	Disadvantages
Synthesis of precursors	Solid-state	Simple operation	Usually requires high temperature and high pressure
	Co-precipitation	Milder conditions	Complex process
	Sol–gel	Better sample uniformity	Complex operation
	Pechini	Wide pH range	Poor control of morphology
	Hydrothermal	Milder reaction conditions	Difficult to synthesize on a large scale
	Flux	High product purity, uniform nanostructures	
Nitridation	Ammonolysis	Traditional and reliable method	Dangerous, need exhaust gas treatment
	Without using NH_3	Relatively safe	Strict requirements on precursors

exhibits no specific morphology. These crystals were further heated in molten LiCl under the NH_3 flow to form regular $LaTaON_2$ cuboids. It was found that this OA growth process is affected by electrostatic repulsion and van der Waals attraction. Meanwhile, the evaporation of LiCl flux induces a supersaturated liquid environment, which promotes the assembly of growth units into regular crystal particles. Although the resulting single crystals are of micrometer-size, this method may also be used to obtain well-defined nanostructures.

4. Visible-light-driven photocatalytic activity

As mentioned in former sections, perovskite-type rare earth oxynitrides containing d^0-type transition metal ions are promising photocatalysts that can respond to visible light. There have been many photocatalytic studies based on rare earth oxynitrides. According to the literature, $LaTiO_2N$ has a bandgap of 2.1 eV and can absorb light with wavelengths greater than 600 nm.[47] In addition, $LaZrO_2N$,[48] $LnTaON_2$ (Ln = La,[49] Ce,[14] Pr[50]), and $LaW(O,N)_3$[51] have favorable optical bandgaps and are suitable for visible-light-driven photocatalytic water splitting. In this reveiw, the photocatalytic activity of water splitting using various rare earth oxynitrides under visible light will be summarized.

4.1. $LaMO_2N$ (M = Ti; Zr)

$LaTiO_2N$ is an n-type semiconductor with a bandgap of 2.1 eV and an absorption edge of about 600 nm.[52] The structure diagram is shown in Fig. 2.[53] According to the literature,[53] $LaTiO_2N$ belongs to the orthorhombic space group of *Imma* (#74), whereas $LaZrO_2N$ belongs to the perovskite structure with the orthorhombic space group of *Pnma* (#62). In addition, $LaTiO_2N$ is considered to adopt an $a^-b^-b^-$-type distortion, in which Ti ions have two different octahedral sites, and the vertices are shared between different octahedra. Its two inclination angles are very close, and both are larger than angles in the *b*-axis. Furthermore, La^{3+} is located in the center of octahedral endpoints in the *c*-axis. However, $LaZrO_2N$ belongs to an $a^+b^-b^-$-type distortion, that is, the two inclination angles are the same, and the adjacent octahedral layers are inclined in phase on one cubic axis, but not on the other axes. In contrast, the octahedron of $LaZrO_2N$ is more twisted than that of $LaTiO_2N$, which may be related to the difference in the relative size and electronegativity between A and B cations.[53]

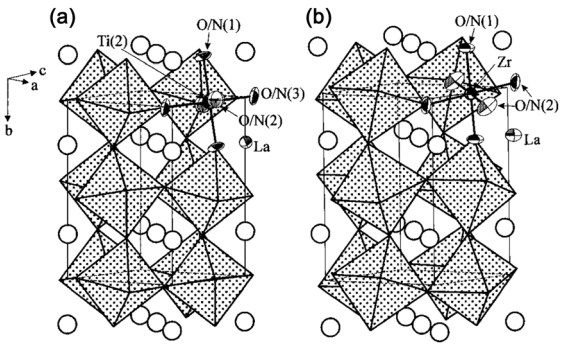

Fig. 2 The structure diagram of $LaTiO_2N$ (a) and $LaZrO_2N$ (b). Reproduced with permission from ref. 53. Copyright 2002, American Chemical Society.

Density functional theory (DFT) calculations can provide a powerful theoretical basis for both bulk and surface structures of a material. Ninova *et al.*[54] used $LaTiO_2N$ as an example to analyse the O/N arrangements on their surface. They first calculated all possible non-equivalent anionic orders in the unit cell of 20 atoms, and determined that the most representative model is the two-dimensional Ti–N–Ti *cis* chain. It is found that the effective masses of electrons and holes of the compounds whose anions are arranged in *cis* form have stronger anisotropy. They further studied the structure of the (001) crystal plane and the arrangement of anions for $LaTiO_2N$, and uncovered that many factors could contribute to the surface sequence, including the chemical composition, degree of polarity, and so on. The most stable surface model is the surface with La as the end and having alternating polarity compensation atomic layers. If the surface is not stable enough, it can be stabilized by electronic and structural reconstruction. The explorations on the structure and composition of the surface will provide insights into improving the photocatalytic activity.

In photocatalytic reactions, methanol is typically used as a sacrificial electron donor and Ag^+ is used as an acceptor to study the reduction of H^+ to H_2 and the oxidation of H_2O to O_2, respectively. Previous studies have shown that $LaTiO_2N$ can generate H_2 and O_2 through water splitting under visible light irradiation, indicating that $LaTiO_2N$ has sufficient oxidation and reduction potential, which can respond to visible light.[55] However, the efficiency of hydrogen and oxygen evolution is often different, making it difficult to carry out the overall water splitting. At the same time, during the process of oxidation and reduction, the degradation of the photocatalyst itself will also occur.[56] The composition of $LaTiO_2N$ is relatively complex, which induces many defects such as N and O vacancies, and La dopants. These defects have the ability to generate additional electronic and optical states, thereby modifying the electronic structure or the band structure. As a result, these defects can serve as composite centers of photo-generated electrons and holes, which is not favorable to water splitting. Based on this, many attempts have been made to solve these problems, such as loading appropriate co-catalysts and partially replacing cations.

Maegli *et al.*[37] explored the effects of $LaTiO_2N$ morphology and CoO_x as co-catalysts on the photocatalytic water oxidation activity. $La_2Ti_2O_7$ were synthesized as precursors by using two methods including the polymerization-complex method and solid-state method, which were called PC-LTO and SS-LTO, respectively. Among them, the shapes of PC-LTO were irregular, while the shapes of SS-LTO were regular, with good dispersibility. Furthermore, SS-LTO had a larger grain size. As shown in Fig. 3, after nitriding the two samples using the ammonolysis method, it was observed that SS-LTON had more voids and retained the morphology of the precursors. In contrast, when using NaCl/KCl as the flux to promote the nitridation process,

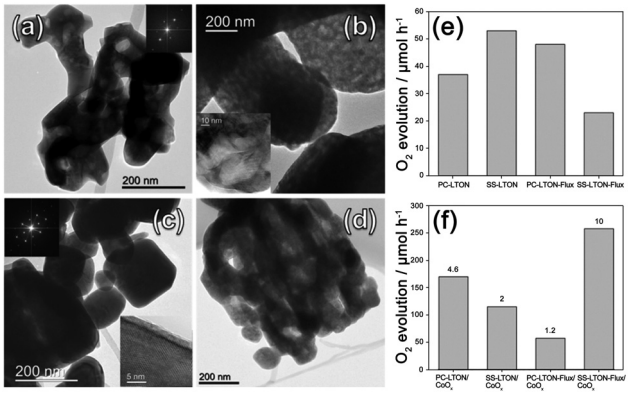

Fig. 3 TEM images of (a) PC-LTON, (b) SS-LTON, (c) PC-LTON-Flux and (d) SS-LTON-Flux. Oxygen evolution rates (e) before and (f) after loading CoO_x as co-catalysts ($\lambda \geq 420$ nm). Reproduced with permission from ref. 37. Copyright 2013, American Chemical Society.

SS-LTON-flux exhibited a skeletal morphology, and its OER rate reached a maximum value of 2600 μmol g^{-1} h^{-1}. In addition, they studied that after dispersing CoO_x as co-catalysts, the dispersibility on SS-LTON-flux was even better, because this skeletal morphology contained many unsaturated surface bonds and provided CoO_x with more nucleation centers, thereby improving the dispersibility of the co-catalyst, which was beneficial for improving the oxygen evolution efficiency.

Later, Li *et al.* obtained hollow spherical $LaTiO_2N$ nanostructures and loaded Pt as the co-catalyst on the sample through the hydrogen reduction method, denoted as Pt/H-LTON, to increase the HER rate.[44] The experimental results implied that the quantum efficiency of this material to generate hydrogen by reducing water under visible light irradiation reaches 3.4% and the corresponding hydrogen evolution efficiency is 960 μmol g^{-1} h^{-1}. As shown in Fig. 4, the particle size of this nanomaterial is small enough, and the best thickness screened by comparison tests is only 7 nm, which is similar to the free path of photo-generated carriers. In such cases, the diffusion distance of photo-generated carriers is shortened so that it can migrate to the surface and avoid being wasted in the relaxation path. For the bulk $LaTiO_2N$ (B-LTON), the surface and volume recombination of photo-generated carriers coexist. However, for Pt/H-LTON, the nanoscale morphology prevents volume recombination, and the introduction of H results in the lattice surface being in a disordered state, thereby inhibiting the surface recombination effectively. Moreover, the authors examined the stability of Pt/H-LTON after 8 days for the HER. The powder XRD results imply that the materials are very stable during the reaction (Fig. 4d).

One drawback of this method is that it can only improve the hydrogen production efficiency and does not help to improve the oxygen production efficiency. Later on, this research group further attempted to load CoO_x on $LaTiO_2N$ and used Fe as dopants to improve the oxygen evolution efficiency,[57] as shown in Fig. 5 and 6. When CoO_x are loaded on $LaTiO_2N$ as co-catalysts, they will form heterojunctions. According to ref. 58, the free path length of the photo-generated carriers in

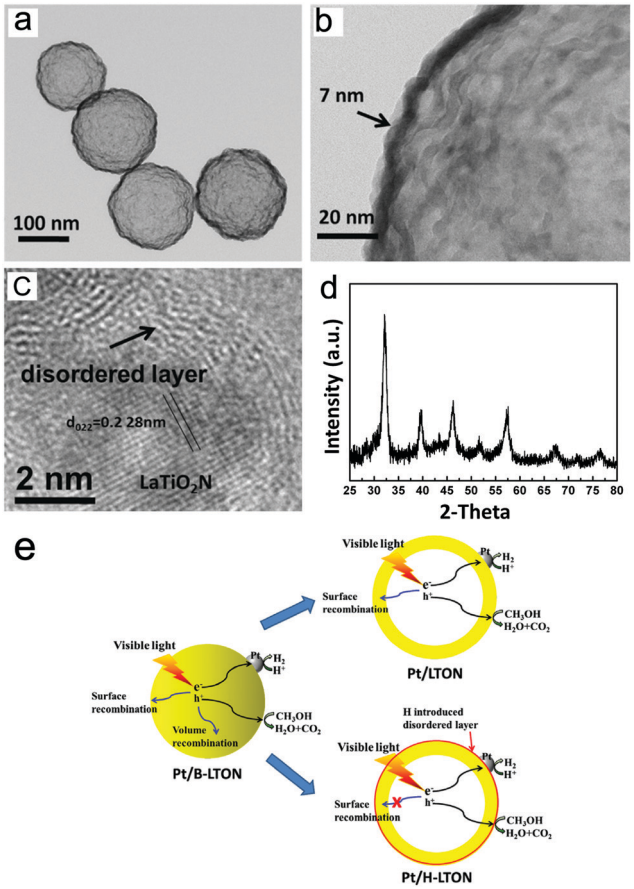

Fig. 4 (a and b) TEM images of hollow spherical $LaTiO_2N$. (c) HRTEM image of $LaTiO_2N$ loaded with Pt by the H_2 reduction method. (d) XRD pattern of Pt/H-LTON after 8 days of H_2 evolution reaction. (e) Schematic diagram of three photocatalysts. Reproduced with permission from ref. 44. Copyright 2015, Elsevier.

$LaTiO_2N$ is about 250 nm. This length is significantly larger than the thickness of nanoscale $LaTiO_2N$. Therefore, photo-generated electrons in $LaTiO_2N$ were migrated to CoO_x with holes, resulting in waste of photo-generated electrons. As defects can confine carriers and also change the band structure, they added Fe dopants at the interstitial position of $LaTiO_2N$ as the defects.

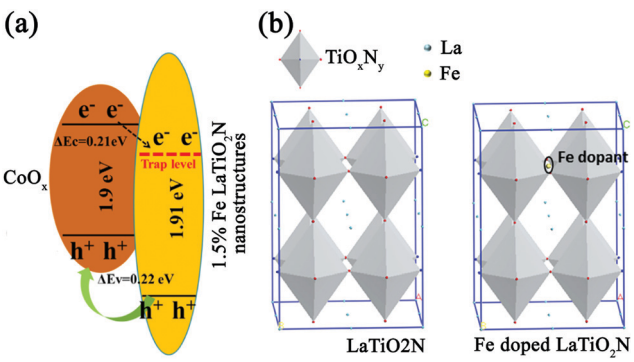

Fig. 5 (a) Band structure of CoO_x/Fe-doped $LaTiO_2N$. (b) Crystal structures of pure $LaTiO_2N$ and Fe doped $LaTiO_2N$. Reproduced with permission from ref. 57. Copyright 2016, Elsevier.

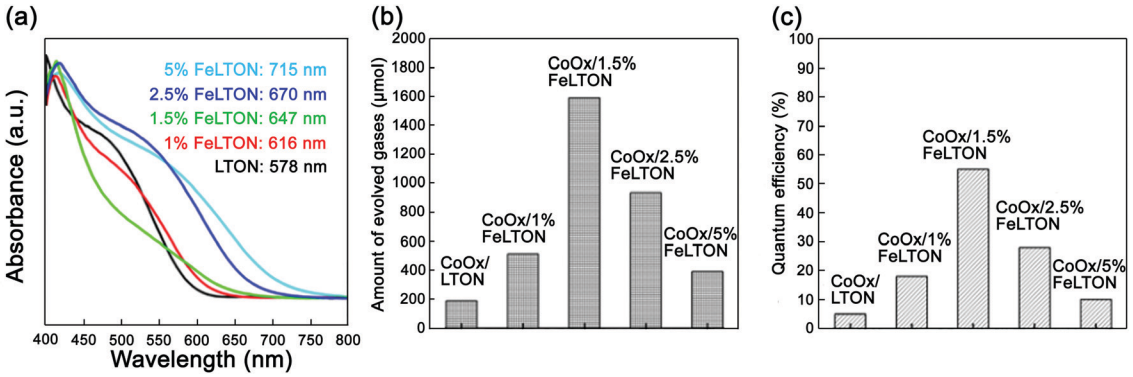

Fig. 6 (a) UV-vis spectra of $LaTiO_2N$ with different Fe doping concentrations. (b) Oxygen production rate of $CoO_x/LaTiO_2N$ with different Fe doping concentrations ($\lambda \geq 420$ nm). (c) The corresponding quantum efficiency. Reproduced with permission from ref. 57. Copyright 2016, Elsevier.

As illustrated in Fig. 5, the ΔE_v (valence band energy) between CoO_x and $LaTiO_2N$ was calculated to be 0.22 eV and the ΔE_c (conduction band energy) was about 0.21 eV, indicating that the energy band arrangement of CoO_x and $LaTiO_2N$ nanostructures was changed. This leads to the separation of photogenerated electrons and holes, thus improving the photocatalytic activity of water oxidation.

As shown in Fig. 6, the UV-vis spectra showed that as the concentration of Fe dopants increased, the absorption edge had significant red-shifts. When the concentration of Fe dopants reached 1.5%, the oxygen evolution rate was the highest, *i.e.*, 1590 μmol g^{-1} h^{-1}, and the corresponding apparent quantum efficiency was 55%. Therefore, by doping Fe in the $CoO_x/LaTiO_2N$ nanostructure, the band arrangement between CoO_x and $LaTiO_2N$ can be adjusted. Meanwhile, the carrier transport can be unblocked and the carrier separation ability can be improved. All these factors are responsible for the improvement of oxygen evolution efficiency.

Thin film materials are often more advantageous than powder materials and thus have been extensively studied. Lawley *et al.* used TiN as the substrate and coated it with MgO for deposition, and finally obtained $LaTiO_xN_y$ ($x + y = 3$) thin films to study the surface modification of the solid–liquid interface during the photocatalytic water splitting.[59] The structure and morphological characteristics of $LaTiO_xN_y$ thin films are shown in Fig. 7. Good boundaries between the layers have been observed in the TEM image. The embedded image indicates that the $LaTiO_xN_y$ and TiN are epitaxially grown on the MgO substrate. The low O/N ratios shown in Fig. 7c are common for epitaxially grown films because of the balance between the crystal quality and total nitrogen content. This research group loaded IrO_2 as co-catalysts on the surface of the exposed $LaTiO_xN_y$ films. The results showed that after loading IrO_2, the degradation rate of the photocatalyst was significantly lower than that of the bare film, which also improved the photocatalytic activity. It is worth noting that they used *ex situ* neutron reflection (NR) and grazing incidence X-ray absorption spectroscopy (GIXAS) to elaborate the reaction that occurs on the surface of the photocatalyst under visible light irradiation and the change of each cation with depth. As shown in Fig. 7d and e, when the bare film is placed in the electrolyte and irradiated with light, the reflectance curve changes little before and after the photoelectrocatalytic reaction. However, after applying an external bias to the film, the reflectance curve fluctuates greatly, which may be responsible for the change in film density. By simulating a one-dimensional scattering length density profile, as shown in Fig. 7f, the TiN layer remains unchanged before and after the reaction, and the loss of N in the first 3 nm below the surface layer is relatively large.

As a result, the neutron reflectometry results show that the process of applying bias and water splitting directly induces changes in film density. In Fig. 7g and h, the X-ray absorption near-edge spectroscopy (XANES) results show that after photoelectrocatalysis, the intensity of La cations of the bare bulk film sample increases and the energy decreases. However, for the La ions on the surface, there is an oxidation transfer to higher energy after catalysis. It can be seen from these two figures that the biggest difference before and after catalysis is the center shift, which indicates that the A cation sites are the main active sites in the water splitting process. The possible reason is that the ionic radius of La is larger than that of Ti and induces the sinking of Ti ions into the subsurface, yielding a surface that is mainly composed of La–O. In Fig. 7i and j, the K edge of Ti does not change, which also confirms that the water splitting process has negligible effects on the valence state of Ti ions. It should be pointed out that when IrO_2 is loaded as a co-catalyst, the position and strength of the L_3 edge before and after the catalysis did not change, which shows that the co-catalyst can play a role in preventing the surface from being modified during the catalytic process.

In this work, through the complementary characterization of neutron reflection and GIXAS, it is revealed that during the catalytic process, the reaction on the catalyst surface and the change of each cation with the change of depth are probed. In other words, it provides effective evidence for the change of the surface structure and the magnitude of the change.

Although $LaZrO_2N$ has a bandgap (2.1 eV) suitable for visible-light-driven photocatalytic reactions, its photocatalysis research was first reported in 2018.[48] The experimental results showed that when loading CoO_x as co-catalysts, $LaZrO_2N$ only

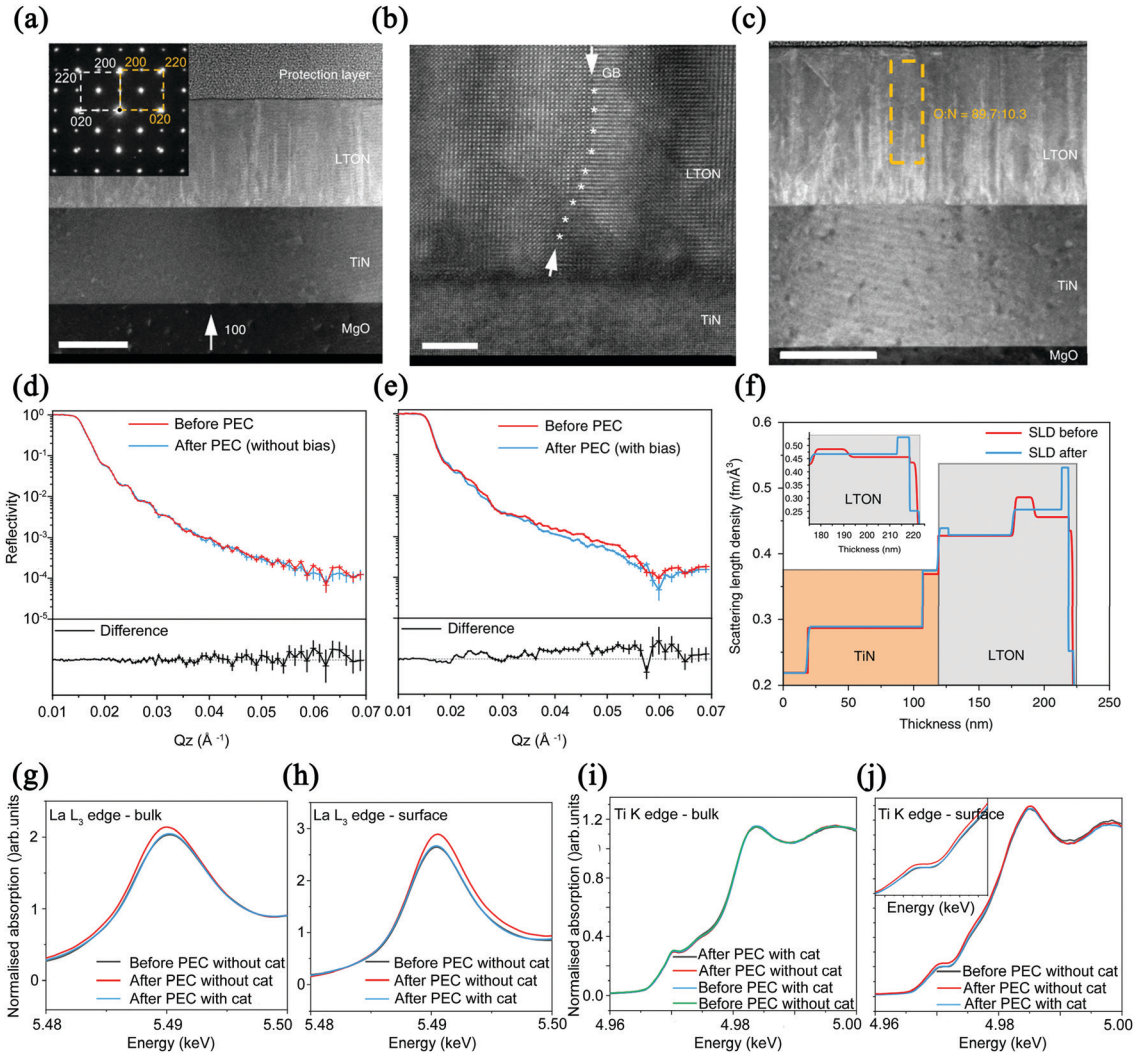

Fig. 7 (a) TEM image of $LaTiO_2N$ cross-section with a scale bar of 100 nm (the selected area electron diffraction as an embedded picture). (b) HAADF image with a scale bar of 5 nm. (c) O/N ratio, the scale bar is 100 nm. Reflectivity diagram of LTON films exposed to electrolyte and light intensity (d) without and (e) with external bias. (f) Simulation of a one-dimensional scattering length density distribution. (g) LTON bulk and (h) surface comparing La before and after PEC. (i) LTON bulk and (j) surface comparing Ti before and after PEC. Reproduced with permission from ref. 59. Copyright 2020, Nature.

exhibited oxygen evolution activity and had no hydrogen evolution ability. Due to the fact that most photocatalysts cannot realize simultaneous hydrogen evolution and oxygen evolution reactions,[60] the concept of a Z-scheme is proposed. Generally speaking, this system includes two types of photocatalysts, and the hydrogen evolution and oxygen evolution reactions occur on the surfaces of the two types of photocatalysts, respectively. Holes exist in the valence band of one photocatalyst, and electrons exist in the conduction band of the other photocatalyst. In the case of a short circuit in the residual charge, overall water splitting can be achieved.[11] Although the current oxygen evolution rate using $LaZrO_2N$ as a photocatalyst is only about 20 μmol g^{-1} h^{-1}, it may be improved by using the Z-scheme.

4.2. $LnTaON_2$ (Ln = La, Ce, Pr)

Based on the literature, $LaTaON_2$ belongs to the orthorhombic space group of *Imma* (#74), as shown in Fig. 8.[49] However, the space group for $CeTaON_2$ is *Pnma* (#62). The formation of distorted perovskite $CeTaON_2$ requires a higher reaction temperature than $LaTaON_2$. It is also easy to form CeO_2 and other phases. CeO_2 is often formed due to its high stability. And the heterogeneous phase may be $Ce(NH_2)_3$ because of the relatively low solubility of Ce.[61] $LaTaON_2$ shows a bandgap of about 1.8 eV, while $CeTaON_2$ shows a similar bandgap of 1.7 eV. Both compounds can in principle respond to visible light. However, as of now, there are no reports about photocatalysis using $CeTaON_2$. $PrTaON_2$ also belongs to the orthorhombic space group of *Pnma*.[50] A previous study showed that the photocatalytic activity of $PrTaON_2$ is not as good as $LaTaON_2$.[50] The author attributed it to excessive defects related to anion vacancies and reduced Ta species generated during the nitridation process. As a result, this review only discusses the photocatalytic activity of $LaTaON_2$.

Liu *et al.* found that when $H_2PtCl_6{\cdot}6H_2O$ and $RuCl_3{\cdot}3H_2O$ were used as precursors to load 0.15% Pt and 0.25% Ru on

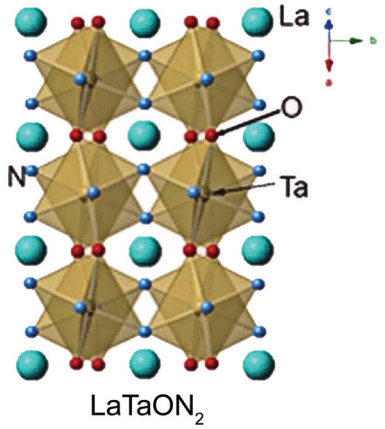

Fig. 8 Structure diagram of $LaTaON_2$. Reproduced with permission from ref. 49. Copyright 2015, John Wiley & Sons, Ltd.

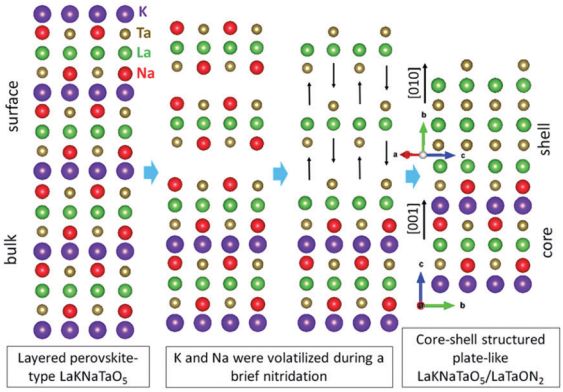

Fig. 10 Side view of the reaction process of the core–shell structure $LaKNaTaO_5/LaTaON_2$, in which N and O atoms are not marked. Reproduced with permission from ref. 45. Copyright 2019, Wiley-VCH.

$LaTaON_2$, the visible-light-driven photocatalytic HER rate of $LaTaON_2$ was 127 μmol g^{-1} h^{-1}.[62] Although $LaTaON_2$ has the ability to absorb visible light, its catalytic activity is apparently poor. Wang *et al.* introduced Zr to the B sites and then improved the photocatalytic activity for water splitting under visible light irradiation.[63] Since Zr^{4+} and Ta^{5+} have similar radii and low electronegativity, Zr^{4+} is a good dopant to form $LaTa_{1-x}Zr_xO_{1+y}N_{2-y}$ ($0 \leq x \leq 0.15$). Experimental results showed that as the doping amount of Zr increases, the unit cell parameters of $LaTaON_2$ become larger and larger, indicating that Zr was randomly added to the sub-lattice of Ta. Although Zr was doped therein, the ability to capture visible light did not decrease, and the bandgap remained at around 2 eV. In addition, the Zr dopant has a significant effect on morphology. With the increasing of Zr doping amount, the surface of $LaTa_{1-x}Zr_xO_{1+y}N_{2-y}$ ($0 \leq x \leq 0.15$) exhibits more pores. One possibility is that Zr is very refractory and thus slows down the grain growth. The BET data show that with increasing pores, the specific surface area has been increased and more active sites are therefore formed, which is more conducive to photocatalytic reactions. From the curve of the photocatalytic hydrogen evolution over time in Fig. 9, it is clear that when $x = 0.1$, *i.e.*, $LaTa_{0.9}Zr_{0.1}O_{1+y}N_{2-y}$, it has the highest photocatalytic activity. The apparent water oxidation quantum efficiency is 0.93%, which is the highest value for $LaTaON_2$ without co-catalysts. The subsequent photoelectrochemical results showed that after doping Zr in $LaTaON_2$, the material showed better charge separation. At the same time, the interface charge transfer resistance was smaller, and the lifetime of electrons was longer. All these factors may be responsible for the enhanced O_2 evolution activity.

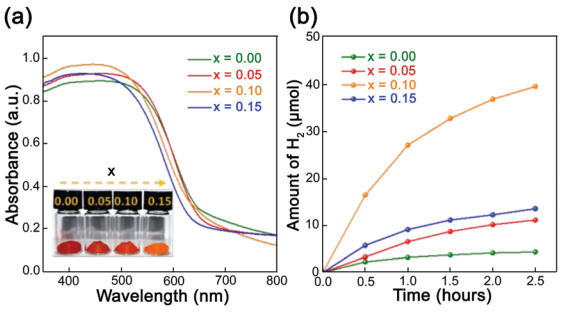

Fig. 9 (a) UV-vis spectra of $LaTa_{1-x}Zr_xO_{1+y}N_{2-y}$ ($0 \leq x \leq 0.15$), the inserted picture is a photo of the sample powder. (b) Curves of photocatalytic hydrogen evolution over time ($\lambda \geq 420$ nm). Reproduced with permission from ref. 63. Copyright 2019, the Royal Society of Chemistry.

In addition to the OER, Wang and co-workers developed an approach to increase the photocatalytic rate of hydrogen evolution effectively.[45] They first used $LaKNaTaON_5$ as the precursor, which contains some volatile components, to synthesize $LaTaON_2$ with a core–shell structure. Such nanostructures effectively improved the HER rate. $LaKNaTaON_5$ has a layered perovskite structure and belongs to the tetragonal crystal system. The atomic distances of the compound along the [001] crystallographic direction are very close to those of $LaTaON_2$ in the [010] crystallographic direction. The experimental results showed that during the nitridation process, the components of K and Na were volatilized, leading to the formation of $LaTaON_2$ along the [010] direction. As a result, $LaKNaTaON_5$ exposing the (001) crystal plane was used as a core, and a shell of $LaTaON_2$ exposing the (010) plane was generated externally, as shown in Fig. 10. This article describes that when the nitriding temperature reaches 1223 K, a pure phase of $LaTaON_2$ can be obtained with an absorption wavelength of 620 nm, which proves that the material can effectively absorb visible light.

In the subsequent photocatalytic experiments, Rh was added as a co-catalyst to detect the photocatalytic activity. As shown in Fig. 11a, core–shell structured $LaKNaTaO_5/LaTaON_5$ exhibited the best visible-light-driven photocatalytic performances for hydrogen evolution. Fig. 11b shows that as the cut-off wavelength increases, the hydrogen evolution rate gradually decreases, and 620 nm is the longest wavelength that this material can respond to. Based on the morphological characteristics of this nanomaterial, the oxynitrides exposing specific crystal planes with a low defect density have a positive effect on photocatalytic activity. Such observations also provide new insights into exploring more efficient photocatalytic materials for water splitting in the future.

Pan *et al.* first synthesized a photocatalyst with an absorption edge greater than 600 nm for the overall water splitting.[49]

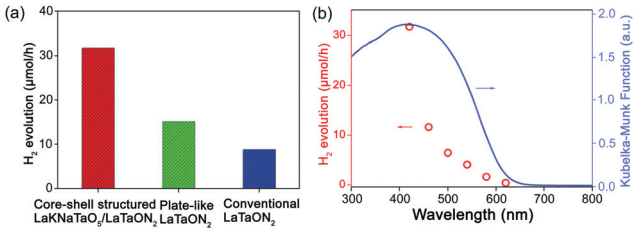

Fig. 11 (a) Hydrogen evolution rates of $LaTaON_2$ with different morphologies. (b) Influence of the incident cut-off wavelength of light on the rate of hydrogen evolution. Reproduced with permission from ref. 45. Copyright 2019, Wiley-VCH.

They used two strategies to prevent the reverse reaction to generate water, and realized the overall water splitting: the first one was to adjust the bandgap by introducing Mg species into $LaTaON_2$ to form a series of $LaMg_xTa_{1-x}O_{1+3x}N_{2-3x}$ (x = 0–2/3) solid solutions; the second was to coat the photocatalyst surface with an amorphous hydroxide layer to control the redox reaction and inhibit the degradation of the photocatalyst, which make some holes to react with N species to generate N_2. They loaded Rh/Cr mixed oxides as the co-catalyst on the surface, simply referred to as $RhCrO_y$, and observed that the photocatalytic activity was the best when x = 1/3. According to the literature,[64] $RhCrO_y$ as a co-catalyst can promote the hydrogen evolution rate while suppressing the O_2 reduction reaction (ORR), *i.e.*, to avoid the occurrence of reverse reactions of water splitting. Accordingly, the authors used common amorphous silicon dioxide and titanium dioxide as the coating layers. These materials may belong to the amorphous hydroxides, denoted as SiOXH and TiOXH. Through a series of comparative tests, it was found that coating with TiOXH can promote overall water splitting. This structure belongs to the core–shell structure. The author believes that by allowing h^+ to enter the oxygen species in the amorphous layer, it can prevent h^+ from accumulating in large amounts in N species on the surface of the photocatalyst, thereby inhibiting the formation of N_2. However, there is no reliable evidence to verify this hypothesis. Despite many advantages of TiOXH/$RhCrO_y$/$LaMg_xTa_{1-x}O_{1+3x}N_{2-3x}$, the apparent quantum yield of overall water splitting is only 0.03% at around 440 nm. As a result, the improvement of photocatalytic activity is still the focus of subsequent research studies.

Later, this research group conducted more detailed research on $LaMg_{1/3}Ta_{2/3}O_2N$.[65] By varying co-catalysts, coating materials and methods, and synthetic methods of precursors, the target of improving photocatalytic activity has been achieved. They first proved that using $RhCrO_x$ as co-catalysts resulted in the highest photocatalytic activity. They then used *in situ* photodeposition to deposit TiO_2 in tetraisopropoxide (TTIP)/H_2O_2 solution to effectively suppress the ORR reaction. The synthesis of the precursor adopts the reverse homogeneous precipitation (RHP) method because the author believed that the sample synthesized by this method may have fewer defects and thus can further improve the photocatalytic activity. Owing to these improvements, the photocatalytic activity has increased by six fold.

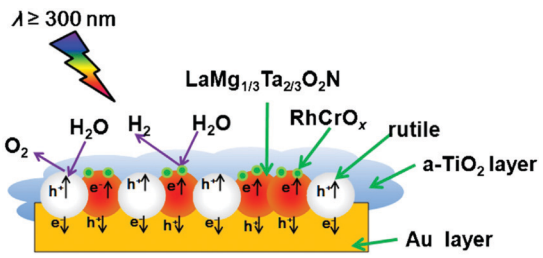

Fig. 12 Schematic diagram of the composition of Z-scheme with $LaMg_{1/3}Ta_{2/3}O_2N$ and rutile. Reproduced with permission from ref. 66. Copyright 2016, Elsevier.

$LaMg_{1/3}Ta_{2/3}O_2N$ can be used for overall water splitting by itself. And it can also be used in the Z-system. Pan *et al.* utilized $RhCrO_x$/$LaMg_{1/3}Ta_{2/3}O_2N$ as a hydrogen evolution photocatalyst (HEP) and rutile as an oxygen evolution photocatalyst (OEP).[66] The results implied that the activity was improved compared to those of the individual components. As shown in Fig. 12, fixing HEP and OEP on the Au layer and coating a-TiO_2 can prevent the transfer of e^- and h^+ between particles and photo-oxidation of $LaMg_{1/3}Ta_{2/3}O_2N$, and thus inhibit the formation of N_2 to achieve the overall water splitting.

4.3. $LaW(O,N)_3$

For $LaW(O,N)_3$, the most common composition is $LaWO_{0.6}N_{2.4}$. According to the literature,[51] tetragonal $LaWO_{0.6}N_{2.4}$ can be formed after nitriding the triclinic $La_2W_2O_9$. As an n-type semiconductor, $LaWO_{0.6}N_{2.4}$ exhibits a photocatalytic water splitting ability to generate oxygen. Although UV-vis spectral data show that it has no obvious absorption edge in the visible light region of 300–800 nm, a trend of increasing absorption can be observed. On one hand, it may be due to the hybridization of the O 2p and N 2p orbitals; on the other hand, it may be owing to the accumulation of a large amount of reduced tungsten (W^{5+} and W^{4+}) and metallic tungsten in the tungsten-based metal oxynitride, which can form a large number of defects in the bandgap. The experimental results showed that the W-containing oxynitrides could be used in photocatalytic reactions under visible light to promote water splitting to produce O_2. However, at the same time, N_2 would also be produced, which can be attributed to photocorrosion. Due to the lack of active sites for oxygen evolution on the surface of the photocatalysts, photo-generated holes are accumulated and reacted with N^{3-} to form N_2, *i.e.*, photocorrosion. The corresponding reaction formulae of this process are shown as follows:

$$2N^{3-} + 6h^+ \rightarrow N_2 \quad (5)$$

$$2O^{2-} + 4h^+ \rightarrow O_2 \text{ (from photocorrosion)} \quad (6)$$

$$2H_2O + 4h^+ \rightarrow 4H^+ + O_2 \text{ (from water oxidation)} \quad (7)$$

It is evident from these equations that the ratio of O_2/N_2 produced during the reaction is similar to the ratio of O/N in the compound. Compared to other W-containing metal oxynitrides, $LaWO_{0.6}N_{2.4}$ produces a higher ratio of O_2/N_2, probably because its 4f orbit is completely empty. The author proposed that if the 4f orbital is partially filled, it may become a composite center

Table 2 A simple comparison of visible-light-driven photocatalytic hydrogen and oxygen evolution rates of perovskite-type oxynitrides

Material	Co-catalyst (loading amount)	Reaction solution	Irradiation condition	Wave length	Activity (μmol g^{-1} h^{-1}) H_2	O_2	Ref.
$CaTaO_2N$	Rh–Cr bimetallic oxide (+1 wt% Ti oxyhydroxide)	Distilled water	300 W Xe	≧300 nm	60	30	67
$SrTaO_2N$	Pt (3 wt%)	Methanol	300 W Xe	>420 nm	100		68
$BaTaO_2N$	Pt (3 wt%)	Methanol	300 W Xe	>420 nm	75		68
$BaNbO_2N$	CoO_x (2 wt%)	30 mM $AgNO_3$	300 W Xe	>600 nm		250	69
$LaTa_{0.9}Zr_{0.1}O_{1+y}N_{2-y}$	CoO_x (2 wt%)	0.05 M $AgNO_3$	300 W Xe	>420 nm	360		63
	Pt (1 wt%)	0.05 M Na_2SO_3				240	
$LaMg_{1/3}Ta_{2/3}O_2N$	$RhCrO_x$ (0.5 wt%)	Pure water	300 W Xe	≧300 nm	110	55	65
$LaZrO_2N$	CoO_x (3 wt%)	10 mM $AgNO_3$	300 W Xe	>400 nm		20	70
$LaTiO_2N$	Fe (1.5%)–CoO_x (7 wt%)	0.2 M $AgNO_3$	300 W Xe	>420 nm		1590	57
$LaTiO_2N$	Pt–H	10 vol% Methanol	300 W Xe	>420 nm	960		44

of photo-generated electrons and holes, the result of which is to inhibit the transport of photo-generated carriers and to reduce the photocatalytic activity.

Table 2 summarizes the visible-light-driven photocatalytic water splitting performances of all perovskite-type oxynitrides reported to date. It is evident that the performances of rare earth oxynitrides are promising among all perovskite-type oxynitrides.

5. Theoretical prediction of phases

In addition to the perovskite-type rare earth oxynitrides shown in the above section, from a theoretical basis, many other rare earth oxynitrides can exist in stable forms. To predict the stability of rare earth oxynitrides, tolerance[71] and octahedral[72] factors are usually used. Li *et al.*[73] used an algorithm based on ionic radius to make a prediction. The results are shown in Table 3. Although it is generally believed that N and O in oxynitrides are arranged randomly, such a statement is still under debate. Nitrogen anions have a greater negative charge and larger ionic radius than oxygen anions, and oxynitrides can form perovskite structures that cannot be formed in perovskite oxides.

Table 3 The possibility of the formation of perovskite-type rare earth oxynitrides

Site		A-site Eu^{2+}	Sc^{3+}	Y^{3+}	La^{3+}	Pr^{3+}	Nd^{3+}	Sm^{3+}
B-site	Si^{4+}		N	N	N	N	N	N
	Ge^{4+}		N	N	N	N	N	N
	Sn^{4+}		N	P	P	P	P	N
	Ti^{4+}		N	P	S/P	P	S/P	N
	Zr^{4+}		N	P	S/P	S/P	S/P	S/P
	Hf^{4+}		N	P	P	P	P	N
	Mn^{4+}		N	N	N	N	N	N
	Fe^{4+}		N	P	P	P	P	P
	Co^{4+}		N	N	N	N	N	N
	V^{4+}		N	P	S^b/P	P	S/P	P
	Nb^{4+}		N	P	P	P	P	N
	Ta^{4+}		N	P	P	P	P	N
	Mo^{4+}		N	P	P	P	P	N
	W^{4+}		N	P	P	P	P	N
	V^{5+}	N	N	N	N	N	N	N
	Nb^{5+}	S/P	N	N	S/P	S/P	N	N
	Ta^{5+}	S/P	N	N	S/P	P	N	N
	Mo^{5+}	P	N	N	P	P	P	N
	W^{5+}	S^b/P	N	N	S^b/P	P	S^b/P	N
	Mo^{6+}	N						
	W^{6+}	P						

S: the compounds which have been synthesized; P: the predicted compounds; N: the perovskite structures which are not stable; ^{b}: the non-integral compounds ($EuWO_{1.58}N_{1.42}$, $LaWO_{0.6}N_{2.4}$, $LaVO_{2.1}N_{0.9}$, and $NdWO_{0.8}N_{2.2}$). Reproduced with permission from ref. 73. Copyright 2013, the Royal Society of Chemistry.

Using tolerance and octahedral factors to evaluate the formation of perovskite oxynitrides can determine whether the reasons for the current few types of such compounds are due to structural instability or synthetic difficulty, which provides clear guidance for the future synthesis of new perovskite oxynitrides. For instance, for potential candidates such as $YSiO_2N$ and $YGeO_2N$, their perovskite structure is proposed to be not stable enough, while $YTiO_2N$ may be synthesized. Strikingly, Y^{3+}, Pr^{3+}, and Nd^{3+} and Hf^{4+}, Fe^{4+}, and Sn^{4+} should form some perovskite nitrogen oxides, but these compounds have not been synthesized yet. It is clear that the calculation of the tolerance and octahedral factors using the ionic radius and the prediction of corresponding oxynitrides with perovskite structures are a really instructive method, which provides a very clear direction for the exploration of new compounds.

6. Conclusion

Nowadays, the exploration of visible-light-driven photocatalysts has gradually become a research hotspot. A pre-requisite of a visible-light-driven photocatalyst is that it must have a suitable bandgap for the absorption of visible light. Towards this end, perovskite-type rare earth oxynitrides are promising candidates. Although the number of studies is still limited, the current visible-light-driven photocatalytic water splitting performances of rare earth oxynitrides are already good compared to other perovskite-type oxynitrides. By optimizing the synthetic methods and conditions, adding co-catalysts and dopants, controlling morphology and sizes, and fabricating nanostructures and nanocomposites, effective separation and migration of photo-generated electrons and holes were achieved, and the competitive recombination of electrons and holes can also be reduced.

Despite the success, the bulk and surface structures of rare earth oxynitrides, and the details of photocatalytic water splitting in these systems, are still not well understood yet. For example, it is often assumed that the N^{3-} and O^{2-} anions are randomly distributed in the crystal lattice. However, the ionic radii, charge, and electronic properties of the two anions are quite different. As a consequence, the ideal random distribution should not exist. The partial aggregate of two anions, especially at the surface, will alter the photocatalytic performances. Such structural information is still not available in current studies. In addition, the change or decomposition of surface structures has been proposed but not well characterized yet. The development of *in situ*/*in operando* characterization techniques such as the *in situ* nuclear magnetic resonance (NMR)[74] technique can accelerate the study of rare earth oxynitrides. Furthermore, many rare earth oxynitride phases are predicted to be stable but are still not synthesized, which will open up great opportunities for future research.

Conflicts of interest

There are no conflicts to declare.

Acknowledgements

J. X. acknowledges the financial support from the National Natural Science Foundation of China (Project 21904071 and 22071115) and the Open Funds (T151904) for the State Key Laboratory of Magnetic Resonance and Atomic and Molecular Physics.

Notes and references

1 C.-J. Liu, U. Burghaus, F. Besenbacher and Z. L. Wang, *ACS Nano*, 2010, **4**, 5517–5526.
2 M. G. Walter, E. L. Warren, J. R. McKone, S. W. Boettcher, Q. Mi, E. A. Santori and N. S. Lewis, *Chem. Rev.*, 2010, **110**, 6446–6473.
3 N. S. Lewis, Basic Research Needs for Solar Energy Utilization, http://www.sc.doe.gov/bes/reports/files/SEU_rpt.pdf.
4 N. S. L. A. D. G. Nocera, *Proc. Natl. Acad. Sci. U. S. A.*, 2006, **103**, 15729–15735.
5 J. O. M. Bockris and J. Klerer, *J. Electrochem. Soc.*, 1973, **120**, 19C.
6 A. Mills and S. Le Hunte, *J. Photochem. Photobiol., A*, 1997, **108**, 1–35.
7 R. Asahi, T. Morikawa, T. Ohwaki, K. Aoki and Y. Taga, *Science*, 2001, **293**, 269.
8 F. E. Osterloh, *Chem. Mater.*, 2008, **20**, 35–54.
9 Y. Wu, P. Lazic, G. Hautier, K. Persson and G. Ceder, *Energy Environ. Sci.*, 2013, **6**, 157–168.
10 T. Takata, C. Pan and K. Domen, *ChemElectroChem*, 2016, **3**, 31–37.
11 T. Takata, C. Pan and K. Domen, *Sci. Technol. Adv. Mater.*, 2015, **16**, 033506.
12 M. Ahmed and G. Xinxin, *Inorg. Chem. Front.*, 2016, **3**, 578–590.
13 Y. Moriya, T. Takata and K. Domen, *Coord. Chem. Rev.*, 2013, **257**, 1957–1969.
14 S. H. Porter, Z. Huang, Z. Cheng, M. Avdeev, Z. Chen, S. Dou and P. M. Woodward, *J. Solid State Chem.*, 2015, **226**, 279–285.
15 M. Yang, J. Oró-Solé, A. Kusmartseva, A. Fuertes and J. P. Attfield, *J. Am. Chem. Soc.*, 2010, **132**, 4822–4829.
16 Y. Lu, C. Le Paven, H. V. Nguyen, R. Benzerga, L. Le Gendre, S. Rioual, F. Tessier, F. Cheviré, A. Sharaiha, C. Delaveaud and X. Castel, *Cryst. Growth Des.*, 2013, **13**, 4852–4858.
17 M. Jansen and H. P. Letschert, *Nature*, 2000, **404**, 980–982.
18 M. Ahmed and G. Xinxin, *Inorg. Chem. Front.*, 2016, **3**, 578–590.
19 L. Yang, H. Zhou, T. Fan and D. Zhang, *Phys. Chem. Chem. Phys.*, 2014, **16**, 6810–6826.
20 S. H. Elder, F. J. DiSalvo, L. Topor and A. Navrotsky, *Chem. Mater.*, 1993, **5**, 1545–1553.
21 P. A. Fuierer and R. E. Newnham, *J. Am. Ceram. Soc.*, 1991, **74**, 2876–2881.
22 L. Shcherbakova, L. Mamsurova and G. Sukhanova, *Russ. Chem. Rev.*, 2007, **48**, 228.
23 J. Takahashi and T. Ohtsuka, *J. Am. Ceram. Soc.*, 1989, **72**, 426–431.
24 B. L. Cushing, V. L. Kolesnichenko and C. J. O'Connor, *Chem. Rev.*, 2004, **104**, 3893–3946.
25 A. V. Prasadarao, U. Selvaraj, S. Komarneni and A. S. Bhalla, *J. Mater. Res.*, 1992, **7**, 2859–2863.
26 M. M. Milanova, M. Kakihana, M. Arima, M. Yashima and M. Yoshimura, *J. Alloys Compd.*, 1996, **242**, 6–10.
27 X. Chen, J. Xu, Y. Xu, F. Luo and Y. Du, *Inorg. Chem. Front.*, 2019, **6**, 2226–2238.
28 T. Okubo and M. Kakihana, *J. Alloys Compd.*, 1997, **256**, 151–154.
29 R. Abe, M. Higashi, K. Sayama, Y. Abe and H. Sugihara, *J. Phys. Chem. B*, 2006, **110**, 2219–2226.
30 M. Higashi, R. Abe, K. Sayama, H. Sugihara and Y. Abe, *Chem. Lett.*, 2005, **34**, 1122–1123.
31 S. Sato, T. Murakata, H. Yanagi, F. Miyasaka and S. Iwaya, *J. Mater. Sci.*, 1994, **29**, 5657–5663.
32 D. Chen and R. Xu, *Mater. Res. Bull.*, 1998, **33**, 409–417.
33 D. Arney, B. Porter, B. Greve and P. A. Maggard, *J. Photochem. Photobiol., A*, 2008, **199**, 230–235.
34 M. Katsura, *J. Alloys Compd.*, 1992, **182**, 91–102.
35 S. G. Ebbinghaus, H.-P. Abicht, R. Dronskowski, T. Müller, A. Reller and A. Weidenkaff, *Prog. Solid State Chem.*, 2009, **37**, 173–205.
36 T. Takata, D. Lu and K. Domen, *Cryst. Growth Des.*, 2011, **11**, 33–38.
37 A. E. Maegli, S. Pokrant, T. Hisatomi, M. Trottmann, K. Domen and A. Weidenkaff, *J. Phys. Chem. C*, 2013, **118**, 16344–16351.
38 A. Gomathi, S. Reshma and C. N. R. Rao, *J. Solid State Chem.*, 2009, **182**, 72–76.
39 D. Ostermann, H. Jacobs and B. Harbrecht, *Z. Anorg. Allg. Chem.*, 1993, **619**, 1277–1282.

40 N. Arumugam, A. Hönnerscheid and M. Jansen, *Z. Anorg. Allg. Chem.*, 2003, **629**, 939–941.
41 Y. Cohen and I. Riess, *J. Mater. Sci. Eng. B*, 1994, **25**, 197–202.
42 R. Aguiar, D. Logvinovich, A. Weidenkaff, H. Karl, C. W. Schneider, A. Reller and S. G. Ebbinghaus, *Mater. Res. Bull.*, 2008, **43**, 1376–1383.
43 M. Sakar, R. M. Prakash, K. Shinde and G. R. Balakrishna, *Int. J. Hydrogen Energy*, 2020, **45**, 7691–7705.
44 Y. Li, X. Cheng, X. Ruan, H. Song, Z. Lou, Z. Ye and L. Zhu, *Nano Energy*, 2015, **12**, 775–784.
45 X. Wang, T. Hisatomi, Z. Wang, J. Song, J. Qu, T. Takata and K. Domen, *Angew. Chem., Int. Ed.*, 2019, **58**, 10666–10670.
46 J. Zhou, C. Zhou, Z. Shi, Z. Xu, S. C. Yan and Z. Zou, *J. Mater. Chem. A*, 2018, **6**, 7706–7713.
47 A. Kasahara, K. Nukumizu, T. Takata, J. N. Kondo, M. Hara, H. Kobayashi and K. Domen, *J. Phys. Chem. B*, 2003, **107**, 791–797.
48 A. P. Black, H. Suzuki, M. Higashi, C. Frontera, C. Ritter, C. De, A. Sundaresan, R. Abe and A. Fuertes, *Chem. Commun.*, 2018, **54**, 1525–1528.
49 C. Pan, T. Takata, M. Nakabayashi, T. Matsumoto, N. Shibata, Y. Ikuhara and K. Domen, *Angew. Chem., Int. Ed.*, 2015, **54**, 2955–2959.
50 M. Hojamberdiev, M. F. Bekheet, J. N. Hart, J. J. M. Vequizo, A. Yamakata, K. Yubuta, A. Gurlo, M. Hasegawa, K. Domen and K. Teshima, *Phys. Chem. Chem. Phys.*, 2017, **19**, 22210–22220.
51 K. Kawashima, M. Hojamberdiev, H. Wagata, E. Zahedi, K. Yubuta, K. Domen and K. Teshima, *J. Catal.*, 2016, **344**, 29–37.
52 M. Yashima, M. Saito, H. Nakano, T. Takata, K. Ogisu and K. Domen, *Chem. Commun.*, 2010, **46**, 4704–4706.
53 S. J. Clarke, B. P. Guinot, C. W. Michie, M. J. C. Calmont and M. J. Rosseinsky, *Chem. Mater.*, 2002, **14**, 288–294.
54 S. Ninova and U. Aschauer, *J. Mater. Chem. A*, 2017, **5**, 11040–11046.
55 N. Nishimura, K. Maeda, T. Takata, D. Lu, J. Kubota and K. Domen, *Bull. Chem. Soc. Jpn.*, 2013, **86**, 540–546.
56 A. Kasahara, K. Nukumizu, G. Hitoki, T. Takata, J. N. Kondo, M. Hara, H. Kobayashi and K. Domen, *J. Phys. Chem. A*, 2002, **106**, 6750–6753.
57 Y. Li, F. Li, X. Li, H. Song, Z. Lou, Z. Ye and L. Zhu, *Nano Energy*, 2016, **19**, 437–445.
58 R. B. Singh, H. Matsuzaki, Y. Suzuki, K. Seki, T. Minegishi, T. Hisatomi, K. Domen and A. Furube, *J. Am. Chem. Soc.*, 2014, **136**, 17324–17331.
59 C. Lawley, M. Nachtegaal, J. Stahn, V. Roddatis, M. Dobeli, T. J. Schmidt, D. Pergolesi and T. Lippert, *Nat. Commun.*, 2020, **11**, 1728.
60 R. Abe, *J. Photochem. Photobiol., C*, 2010, **11**, 179–209.
61 N. Cordes and W. Schnick, *Chem. – Eur. J.*, 2017, **23**, 11410–11415.
62 M. Liu, W. You, Z. Lei, T. Takata, K. Domen and C. Li, *Chin. J. Catal.*, 2006, **27**, 556–558.
63 Y. Wang, S. Jin, G. Pan, Z. Li, L. Chen, G. Liu and X. Xu, *J. Mater. Chem. A*, 2019, **7**, 5702–5711.
64 K. Maeda, K. Teramura, H. Masuda, T. Takata, N. Saito, Y. Inoue and K. Domen, *J. Phys. Chem. B*, 2006, **110**, 13107–13112.
65 C. Pan, T. Takata and K. Domen, *Chem. – Eur. J.*, 2016, **22**, 1854–1862.
66 Z. Pan, T. Hisatomi, Q. Wang, M. Nakabayashi, N. Shibata, C. Pan, T. Takata and K. Domen, *Appl. Catal., A*, 2016, **521**, 26–33.
67 J. Xu, C. Pan, T. Takata and K. Domen, *Chem. Commun.*, 2015, **51**, 7191–7194.
68 D. Yamasita, T. Takata, M. Hara, J. N. Kondo and K. Domen, *Solid State Ionics*, 2004, **172**, 591–595.
69 T. Hisatomi, C. Katayama, K. Teramura, T. Takata, Y. Moriya, M. Katayama, H. Nishiyama, T. Yamada and K. Domen, *ChemSusChem*, 2014, **7**, 2016–2021.
70 A. P. Black, H. Suzuki, M. Higashi, C. Frontera, C. Ritter, C. De, A. Sundaresan, R. Abe and A. Fuertes, *Chem. Commun.*, 2018, **54**, 1525–1528.
71 C. J. Bartel, C. Sutton, B. R. Goldsmith, R. Ouyang, C. B. Musgrave, L. M. Ghiringhelli and M. Scheffler, *Sci. Adv.*, 2019, **5**, eaav0693.
72 W. Travis, E. N. K. Glover, H. Bronstein, D. O. Scanlon and R. G. Palgrave, *Chem. Sci.*, 2016, **7**, 4548–4556.
73 W. Li, E. Ionescu, R. Riedel and A. Gurlo, *J. Mater. Chem. A*, 2013, **1**, 12239–12245.
74 X. L. Wang, W. Liu, Y.-Y. Yu, Y. Song, W. Q. Fang, D. Wei, X.-Q. Gong, Y.-F. Yao and H. G. Yang, *Nat. Commun.*, 2016, **7**, 11918.